
Article:
Wang, L.G., Ge, R. and Chen, X. orcid.org/0000-0001-8073-5741 (2022) Establishing an oblique impact breakage master curve using a DEM bonded contact model. Computers and Geotechnics, 145. 104668. ISSN 0266-352X

https://doi.org/10.1016/j.compgeo.2022.104668

Computers and Geotechnics 145 (2022) 104668

Contents lists available at ScienceDirect

Computers and Geotechnics

journal homepage: www.elsevier.com/locate/compgeo

Establishing an oblique impact breakage master curve using a DEM bonded contact model

Li Ge Wang [a,b], Ruihuan Ge [b,*], Xizhong Chen [b]

[a] Process Systems Enterprise, Hammersmith, London, UK
[b] Department of Chemical and Biological Engineering, University of Sheffield, UK

ARTICLE INFO

Keywords:
Breakage master curve
Oblique impact
Equivalent velocity
Impact angle
Discrete Element Method (DEM)
Bonded contact model

ABSTRACT

This paper aims to establish a breakage master curve of oblique impact using a DEM bonded contact model. Despite numerous advantages of particle impact breakage by DEM, there exist two major issues in hindering the distinct power of DEM with a fully predictive capacity. The first barrier is the notable discrepancy of breakage probability evaluation, i.e. breakage ratio in experiments and damage ratio in DEM. The second barrier is the lack of an oblique impact model where the breakage probability subject to various impact angles can be unified. In this work, these two longstanding barriers are addressed by conducting digital twin of impact breakage using a DEM bonded contact model. A newly developed oblique impact model is used to account for the effect of impact angle. The equivalent velocity proposed in the oblique impact model is shown to successfully establish a remarkable breakage master curve for all the impact angles.

1. Introduction

Particle impact breakage including attrition, chipping and fragmentation is typically encountered in geotechnical engineering such as rock falls and landslides (Gentilini et al., 2012; Giacomini et al., 2009; Ruiz-Carulla et al., 2017). The consequence of impact breakage depends on several governing factors amongst which the stressing magnitude and particle mechanical properties are dominant (Wang et al., 2021b). In terms of the stressing magnitude, the impact velocity has been widely adopted as a rule of thumb to distinguish the breakage patterns. Specifically, the lower impact velocity results in attrition or chipping whereas the higher impact velocity leads to fragmentation (Salman et al., 2003). As for the particle mechanical properties, the brittleness, i.e. the ratio of hardness to fracture toughness serves as an indicator and a high brittleness index usually signifies a brittle substance (Meier et al., 2009). Apart from this, particle size and particle shape can play important roles in impact breakage. The early attempt of impact breakage was conventionally made by experimental approaches, where only a limited amount of governing factors can be examined for sensitivity analysis. Alternatively, several researchers made considerable efforts to incorporate these key governing factors by means of a theoretical approach. The development of mechanistic-based chipping models was performed with the aim to build the relationship between mechanical properties and particle volume loss (Evans et al., 1978; Evans and Wilshaw, 1976; Ghadiri and Zhang, 2002). The common ground for the chipping model development lies in the physical foundation of nano-indentation fracture mechanics. In contrast, the marked difference is the varying exponent on the impact velocity, which has been a moot point in the literature. The developments of fragmentation model were made in the format of statistical distribution such as Weibull distribution and logistic distribution. (Salman et al., 1995; Tavares and King, 1998; Vogel and Peukert, 2003). The advantage of these theoretical models is to provide mechanistic insights into the particle breakage processes and to reduce the amount of experimental efforts. However, the particle dynamics including particle impact velocity, impact angle and impact number at the short intervals of process are not straightforward and cannot be readily obtained from experiments.

To address these barriers, a computational based approach, i.e. Discrete Element Method (DEM) has been widely used to capture the particle dynamics subject to stressing events relevant to a breakage process. DEM simulations of particle breakage subject to impact loadings are usually conducted to evaluate the breakage propensity and size distribution after impact incidents. Early attempt of single particle breakage induced by normal impact was carried out using 2D DEM (Potapov and Campbell, 1994). The agglomerates were assembled by continuous contacts of convex polygons. Three parameters including Poisson ratio, characteristic strain of the particle and impact energy are

* Corresponding author.
E-mail address: R.Ge@sheffield.ac.uk (R. Ge).

https://doi.org/10.1016/j.compgeo.2022.104668
Received 19 August 2021; Received in revised form 5 January 2022; Accepted 10 February 2022
Available online 9 March 2022

Nomenclature

a	Fitting parameter, –
A	Cross-sectional area, m^2
b	Intermediate diameter, m
B	Number of bonded contact, –
c	Shortest diameter, m
d	Displacement, m
D_1, D_2	Particle size, m
D_r	Damage ratio, –
e	coefficient of restitution, –
E	Young's modulus, Pa
F	Force, N
f_s	Form factor, –
f_{Mat}	Material properties, –
G	Shear modulus, Pa
H	Hardness, MPa
I	Moment of inertia, N m
k	Impact number, –
K	Stiffness matrix, –
K_c	Fracture toughness, Pa $m^{0.5}$
L_b	Bond length, m
m	Mass, g
M	Moment, N m
M_m	Mother particles mass, g
M_{de}	Debris particle mass, g
n	Population density of length function, m^{-3}
n_p	Total number of particles, –
n_c	Total number of inter-particle bonds, –
N	Number of breakage events, –
P_x	Breakage probability of particle size x, –
P_i	Position, m
R	Particle radius, mm
r_b	Bond radius, mm
S	Strength, MPa
t	Time, s
u	Displacement, m
v	Velocity, m s^{-1}
w_i	Mass fraction, –
$W_{m,kin}$	Mass specific impact kinetic energy, J kg^{-1}
$W_{m,min}$	Threshold kinetic energy, J kg^{-1}
x	Particle size, m

Greek symbols

ν	Poisson's ratio, –
α	Constant, –
β	Constant, –
ε	Porosity, –
μ	Friction coefficient, –
ω	Angular velocity, rad s^{-1}
ρ	Density, kg m^{-3}
σ	Stress, Pa
τ	Shear stress, Pa
ξ	Time step factor, –
η	Contact radius multiplier, –
ϕ	Timoshenko shear coefficient, –
θ	Angular, degree
λ	Bond radius multiplier, –
ψ	'Equivalent' normal impact velocity coefficient, –

studied. The impact energy leads to the biggest change in the size distribution of fragments. Thornton et al. presented a 3D simulation of spherical agglomerates consisting of autoadhesive particles impacting a target wall (Thornton et al., 1999). The evolution process of impact breakage was divided into the loading and unloading stages. The loading stage was initiated by a damage zone involving irreversible deformation of the microstructure, interparticle sliding and randomly distributed mirco-crack formation. Over the unloading course, the micro-crack formation was further extended by coalescence, leading to subsequent fracture along half-meridian planes. Kun et al. and co-worker focused their attention on fragmentation of brittle materials at both 2D and 3D levels (Carmona et al., 2008; Kun and Herrmann, 1999, 1996). 3D DEM simulation of fragmentation process was performed to study the breakage of spheres inside which the agglomerated particles are connected by beam-truss elements (Carmona et al., 2008). The resulting fragmentation mass distribution was described by a power law regime for small fragments and a broad peak for large fragments fitted by a two-parameter Weibull distribution. The effect of impact angle via DEM simulation was studied on the agglomerates breakage (Moreno et al., 2003). The results show that the normal component of the impact velocity plays a dominant role in controlling the breakage of contacts. Most importantly, it was concluded that the breakage pattern is dependent on the tangential component of the impact velocity. Similar research about impact breakage of agglomerates under different conditions has also been reported (Tong et al., 2010, 2009).

Despite the plethora of DEM studies of particle breakage by various contact models, there remain two pivotal barriers in unleashing the power of DEM with a fully predictive accuracy. The first barrier is the notable discrepancy of breakage probability evaluation between the experimental and numerical tests. The breakage probability is generally used to describe the fraction of particles which are broken in the impact event (Vogel and Peukert, 2003). The breakage probability is experimentally characterised by mass loss on particle size basis (Li et al., 2020) whereas the percentage of broken bond number in DEM is used to evaluate the breakage probability (Ye et al., 2021). Because of this discrepancy, the direct comparison of breakage probability between the experimental and numerical results has barely been available. As a result, the model validation of DEM simulation of impact breakage has not been fully accomplished. Secondly, despite substantial oblique impact breakage research using DEM, a model to predict the effect of impact angle on the breakage probability is still scarce. Although the breakage master curve was successfully constructed irrespective of different materials (Vogel and Peukert, 2003), the incorporation of impact angle in a unified master curve presents a grand challenge. The difficulty of constructing a breakage master curve considering various impact angles lies in the fact that there is no single breakage model to account for the effect of tangential component velocity.

In this work, we present a hybrid numerical and theoretical study to establish a breakage master curve based on DEM simulation of oblique impact. A bonded contact model rooted from Timoshenko beam theory is deployed to represent the connection between neighbouring constitutive particles. Two key obstacles identified from the previous DEM study of particle impact breakage are addressed. The first obstacle is the indirect comparison between damage ratio in DEM and breakage ratio in experiments. The lack of a unified breakage criterion results in a great difficulty in calibrating the DEM simulation of impact breakage and further assessment with theoretical breakage models. The breakage probability of bonded particles is calculated using the Breadth-First search algorithm, thus the size distribution of fragments after impact breakage can be calculated and analysed. The second obstacle is the futility of existing breakage models in predicting the breakage probability subject to impact loading. The unification of breakage probability under various impact angles is achieved using equivalent velocity in a newly developed breakage model. The universality of equivalent

velocity is demonstrated via DEM simulations of particle impact breakage under varying impact angles.

2. DEM bonded contact model

For modelling the breakage characteristics in DEM, the granular material is envisaged as an assembly of bonded particles. A series of bonded contact models are available in the literature to describe the mechanical behaviour of granular materials from microscopic scale. These bonded contact models include but not limited to parallel bond model and Edinburgh Bonded Particle Model (Brown et al., 2014; Potyondy and Cundall, 2004; Shen et al., 2016). The notable difference among these constitutive bonded contact models lies in the assumption of governing equations to describe the bond evolution from a structured (bonded) state to a destructured (unbonded) state (Jiang et al., 2014). The bonded contact model used in the present work is the recently developed Edinburgh Bonded Particle Model (EBPM) based on Timoshenko beam theory (Brown et al., 2014). This model can transit the axial, shear and bending behaviours. In this section, the governing equations and the numerical setup of EBPM are firstly presented. The generation procedures of bonded particles and calibrated parameters used in this work are then described below.

The illustration of a contact bond between two neighboring particles is schematically depicted in Fig. 1. Notably, only one bond is allowed between the two neighboring particles and it will not be reverted once the bonded contact is broken. Once the bond is broken by the failure criterion, the neighboring particles start to follow the Hertz-Mindlin model (Mindlin and Deresiewicz, 1953; Tsuji et al., 1992). For controlling the bond formation and bond geometry, there are two bond fabrication parameters: contact radius multiplier (η) and bond radius multiplier (λ). In two neighboring particles, the bond domain is determined using a contact radius multiplier (η) of which the value is beyond one. The two neighboring particles are bonded if there is an overlap between the multiplied contact radius. In this work the bond contact radius multiplier (η) is defaulted as 1.1 to create virtual radii so that a contact bond can be generated between any two neighboring particles. The bond radius multiplier, λ, defines the radius of each bond (r_b) according to:

$$r_b = \lambda \bullet \min(\mathrm{r_A}, \mathrm{r_B}) \tag{1}$$

where r_A and r_B are the radii of bonded particles A and B respectively. In this work, the bond radius multiplier (λ) is set as 0.5.

For a bonded contact, a circular beam element is assumed to rigidly connect the two particles and each bond element is assumed straight in three-dimensional space in terms of formation. The behaviour of the bond is assumed to follow Timoshenko beam theory (Timoshenko, 1922). It is assumed that the beam element connects the centres of the two particles and thus each end of the bond shares the same six degrees of freedom as the particle.

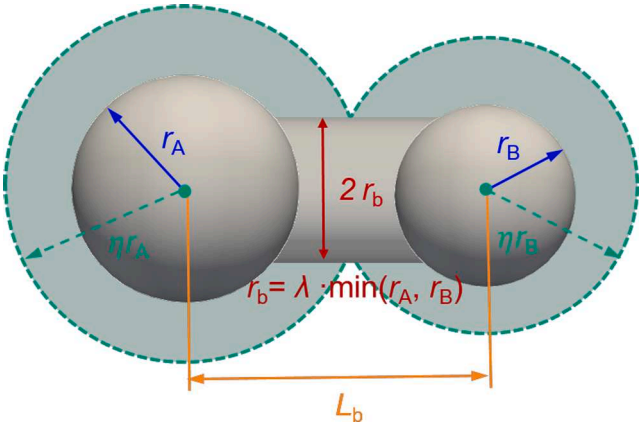

Fig. 1. Illustration of two constitutive particles connected by a bond. The solid circle illustrates the actual particles, while the broken circle and overlap are used to detect bonded contact (r_A and r_B are particle radius, L_b is bond length, r_b is bond radius).

In Fig. 1, the centres of particles A and B are connected by a single bond. L_b and r_b denote the length and radius of the bond, respectively. The positions of the two particles are denoted by vectors $\{P_A\}$ and $\{P_B\}$ in the global Cartesian coordinate system (X, Y, Z).

$$\{P_i\} = \{X_i Y_i Z_i\} i = A, B \tag{2}$$

The length of the bond L_b is given:

$$L_b = \|P_A - P_B\| \tag{3}$$

Timoshenko beam theory is used to relate the internal forces and moments to the particle displacements and rotations. The increments of the internal forces and moments in each time step are determined from the incremental displacements and rotations at the bond ends using the Timoshenko beam theory. This gives:

$$\{\Delta F\} = [K] \bullet \{\Delta \mathrm{u}\} \tag{4}$$

where the incremental force vector $\{\Delta F\}$ and displacement (rotation) vector $\{\Delta u\}$ are

$$\{\Delta F\} = \begin{Bmatrix} \Delta F_{\alpha x} & \Delta F_{\alpha y} & \Delta F_{\alpha z} & \Delta M_{\alpha x} & \Delta M_{\alpha y} & \Delta M_{\alpha z} \\ \Delta F_{\beta x} & \Delta F_{\beta y} & \Delta F_{\beta z} & \Delta M_{\beta x} & \Delta M_{\beta y} & \Delta M_{\beta z} \end{Bmatrix}^T$$

$$\{\Delta u\} = \begin{Bmatrix} \Delta d_{\alpha x} & \Delta d_{\alpha y} & \Delta d_{\alpha z} & \Delta \theta_{\alpha x} & \Delta \theta_{\alpha y} & \Delta \theta_{\alpha z} \\ \Delta d_{\beta x} & \Delta d_{\beta y} & \Delta d_{\beta z} & \Delta \theta_{\beta x} & \Delta \theta_{\beta y} & \Delta \theta_{\beta z} \end{Bmatrix}^T \tag{5}$$

in which $\{\Delta F\}$ contains 12 force (F) and moment (M) increments at the two ends of the bond, $\{\Delta u\}$ contains 12 displacement (d) and rotation (θ) increments at the two ends of the bond, and $[K]$ is a 12x12 tangential stiffness matrix. The internal total force (F) and moments (M) are depicted in Fig. 2. α and β denotes the two ends of the bond, and x, y and z denote the direction of the force in the local coordinate system of the bond. Note that the bonds are not only subjected to the internal force caused by displacements but also to that caused by rotation within neighbouring particles. Furthermore, the bonded contact model is expected to simulate both small and large rigid body rotation upon appropriate assigned values of model parameters.

The tangential stiffness matrix $[K]$ remains constant before failure for small deformation linear elastic bonds and the general form is (Przemieniecki, 1968):

$$[K] = \begin{bmatrix} K_1 & -K_2 & -K_1 & -K_2 \\ K_2 & K_3 & -K_2 & K_4 \\ -K_1 & K_2 & K_1 & K_2 \\ K_2 & K_4 & -K_2 & K_3 \end{bmatrix} \tag{6}$$

where

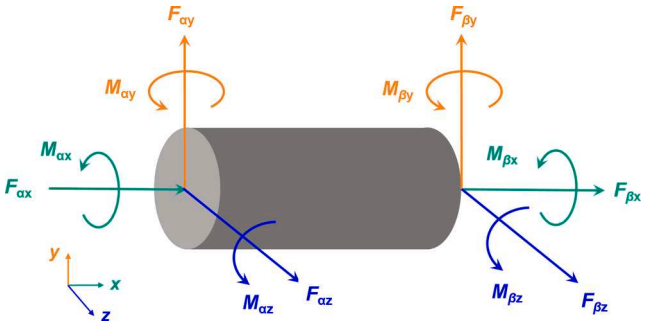

Fig. 2. Forces and moments acting at the ends of a bond in the local coordinate system.

$$[K_1] = \begin{bmatrix} \frac{E_b A_b}{L_b} & 0 & 0 \\ 0 & \frac{12k}{L_b{}^2(1+\phi)} & 0 \\ 0 & 0 & \frac{12k}{L_b{}^2(1+\phi)} \end{bmatrix}$$

$$[K_2] = \begin{bmatrix} 0 & 0 & 0 \\ 0 & 0 & \frac{-6k}{L_b(1+\phi)} \\ 0 & \frac{6k}{L_b(1+\phi)} & 0 \end{bmatrix}$$

$$[K_3] = \begin{bmatrix} \frac{k}{1+\nu_b} & 0 & 0 \\ 0 & \frac{k(4+\phi)}{(1+\phi)} & 0 \\ 0 & 0 & \frac{k(4+\phi)}{(1+\phi)} \end{bmatrix}$$

$$[K_4] = \begin{bmatrix} \frac{-k}{1+\nu_b} & 0 & 0 \\ 0 & \frac{k(2-\phi)}{(1+\phi)} & 0 \\ 0 & 0 & \frac{k(2-\phi)}{(1+\phi)} \end{bmatrix}$$

where $k = \frac{E_b I_b}{L_b}$, E_b is the Young's modulus, ν_b is the Poisson ratio, A_b is the cross-sectional area, I_b is the second moment of area of the bond and $\phi = \frac{f_s 12 E_b I_b}{G_b A_b L_b^2}$ is the Timoshenko shear coefficient; where f_s and G_b are the form factor for shear and the bond's shear modulus respectively.

In terms of small deformation, the bond stress, including total internal forces and moments at the bond ends is given by:

$$\{F\} = \sum \Delta F \tag{7}$$

where $\{F\}$ contains 12 total forces and moments as below:

$$\{F\} = \{ F_{\alpha x} F_{\alpha y} F_{\alpha z} M_{\alpha x} M_{\alpha y} M_{\alpha z} F_{\beta x} F_{\beta y} F_{\beta z} M_{\beta x} M_{\beta y} M_{\beta z} \}^T \tag{8}$$

Bonds are assumed to behave in a linear elastic brittle way; The bond is deemed to fail if the maximum value of any calculated stress exceeds the corresponding strength. The failure criteria include three parameters, i.e., compressive σ_C , tensile σ_T and shear τ. The maximum stresses σ_{Cmax}, σ_{Tmax} and τ_{max} within a bond are defined as follows:

$$\sigma_{Ci} = \left(\frac{F_{\beta x}}{A_b} - \frac{r_b \sqrt{M_{iy}^2 + M_{iz}^2}}{I_b} \right) i = \alpha, \beta \tag{9}$$

$$\sigma_{Cmax} = -min(\sigma_{C\alpha}, \sigma_{C\beta}) \tag{10}$$

$$\sigma_{Ti} = \left(\frac{F_{\beta x}}{A_b} + \frac{r_b \sqrt{M_{iy}^2 + M_{iz}^2}}{I_b} \right) i = \alpha, \beta \tag{11}$$

$$\sigma_{Tmax} = max(\sigma_{T\alpha}, \sigma_{T\beta}) \tag{12}$$

$$\tau_{max} = \frac{|M_{\alpha x}| r_b}{2 I_b} + \frac{4\sqrt{F_{\alpha y}^2 + F_{\alpha z}^2}}{3 A_b} \tag{13}$$

3. Particle assembly and DEM simulation setup

3.1. Constitutive particle assembly

Rigid spherical constitutive particles are considered in the DEM model for simplicity, which have been widely used in a series of DEM compressive and impact loading tests (Ergenzinger et al., 2011; Gilvari et al., 2020; Ouyang et al., 2017). In other words, the constitutive particles do not individually break or degrade but the bonds connecting these constitutive particles can break when suffering from various stressing conditions. A spherical test particle was generated by bonding together a large number of constituent spheres. A random particle assembly with 63% solid fraction was generated using an advancing front particle-packing algorithm (Valera et al., 2015). This generation technique randomly creates particles according to an imposed particle size distribution. As illustrated in Fig. 3, a total of 13,353 primary particles was generated within a 100 mm diameter spherical geometry. According to Brown et al. (Brown et al., 2014), a uniform particle size distribution was used with the minimum (r_{min}) and maximum (r_{max}) radii set equal to 1.15 mm and 2.71 mm, respectively. The inter-particle bonds are generated, and the total number of bonds within the contact radius is 46,754 prior to impact breakage. The characteristics of the particle assembly are tabulated in Table 1.

3.2. Model parameter calibration

The overarching goal of parameter calibration is to find out a workable relationship between microscale model input parameters and the macroscopic deformation behaviours subject to compressive, tensile and impact stressing conditions. In the previous work, the bulk response of a concrete specimen under uniaxial compressive test is compared to those using the Eurocode equations (Brown, 2013). The key performance indicators (KPI), i.e. the ultimate strength, the strain at ultimate strength, the secant bulk modulus and the bulk Poisson's ratio are considered in the model calibration procedure. As the presented bonded contact model in Section 2 has a large amount of input parameters, the first step in the calibration procedure is to identify the most influential parameters through a series of parametric study. The most influential bonded contact parameters are found to be bond Young's modulus, the mean bond tensile and shear strength. In the second step, the model parameters which are required for calibration can be substantially reduced by keeping the majority of the input parameters constant. This is in good agreement of the other literature study using the same bonded contact model for a pellet specimen via uniaxial and diametrical compression tests (Gilvari et al., 2020). The third step is to compare the stress- strain behaviour with DEM concrete specimen with an ultimate compressive strength of 27.9 MPa. It should be noted that the bond tensile strength is a micromechanical strength property, which should be distinguished from the tensile strength of concrete specimen from the bulk response. With an empirical relationship between compressive and tensile strength for brittle concrete-like or rock-like materials (Chhorn et al., 2018), the bulk tensile strength from Brazilian tensile test is calculated as 4.9 MPa, i.e. 17.6 % of the compressive strength, which falls in the common range of tensile strength for conventional brittle materials. The detailed illustration of EBPM model calibration for compressive and tensile tests can be found in Appendix A. Once model parameters are calibrated through the uniaxial compressive tests, the predictive accuracy of DEM bonded contact model can be assured by extending its application to the other stressing events. Following this idea, the calibrated parameters are adopted to simulate the oblique impact breakage of particles over a wide range of impact velocity in the present work.

3.3. Model parameterization

Upon the definition of contact model and constitutive particle

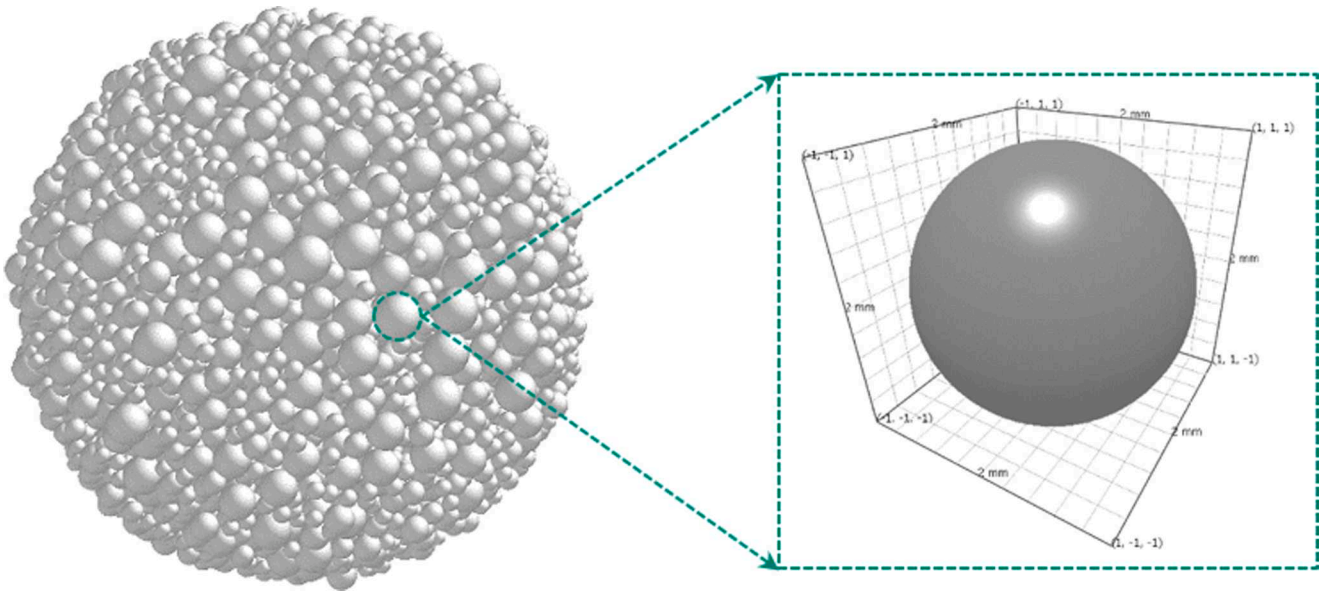

Fig. 3. Initial particle assembly.

Table 1
Characteristics of particle assembly.

Parameter	Description	Value
R	Radius of multi-sphere particle assembly (mm)	50
n_p	Total number of constituent spheres (–)	13,353
n_c	Total number of bonds (–)	46,754
ε	Porosity (–)	0.37
r_{max}	Maximum radius of constituent sphere (mm)	1.71
r_{min}	Minimum radius of constituent sphere (mm)	1.15
r_{av}	Average radius of constituent sphere (mm)	1.43

assembly, the next procedure is to specify input parameters. The EBPM contact model has been successfully calibrated in a variety of stressing paths including the application in axial strain of brittle cylinder samples (Brown et al., 2014), the compressive loading of 3D printed agglomerates and biomass pellets (Ge et al., 2020, 2019, 2017; Gilvari et al., 2020) and tensile test of flexible ring net (Zhu et al., 2020). In this study, the calibrated parameters in the EBPM are referred from (Brown et al., 2014) where satisfactory predictions for brittle-like cylindrical samples were observed in the stress–strain curve. The general issues about developing and validating the calibration methods for DEM can be found in (Coetzee, 2017). The particle bond parameters in EBPM are tabulated in Table 2. For simplicity, the coefficient of variation for the bond strengths is assumed to be zero. The Hertz-Mindlin with no slip contact model was chosen to represent the behaviour for non-bonded contacts. The characteristics of non-bonded parameters are summarized in Table 3. The subscripts p and g represent the properties of particle and geometry, respectively. The criterion of selecting impact target is to ensure the impact breakage of particles is insensitive to the impact target property. In this work the impact platen geometry is assumed to be made from steel which is commonly used for standard mechanical tests.

Table 2
Input value of bond parameters after (Brown, 2013).

Parameter	Description	Value
E_b	Young's modulus (GPa)	28
ν_p	Poisson's ratio	0.2
S_C	Mean compressive strength (MPa)	300
S_T	Mean tensile strength (MPa)	60
S_S	Mean shear strength (MPa)	60
η	Contact radius multiplier	1.1
λ	Bond radius multiplier	0.5

Table 3
Input value of non-bonded parameters (Brown, 2013).

Parameter	Description	Value
E_p	Particle Young's modulus (GPa)	70
ρ_p	Particle density (kg m^{-3})	2650
ν_p	Particle Poisson's ratio	0.25
μ_{sp}	Particle-particle static friction	0.3
e_{rp}	Particle-particle restitution	0.9
μ_{rp}	Particle-particle rolling friction	0.01
E_g	Plate Young's modulus (GPa)	200
ν_g	Plate Poisson's ratio	0.25
e_{pg}	Platen-particle coefficient of restitution	0.7
μ_{sg}	Platen-particle coefficient of static friction	0.35
μ_{rg}	Platen-particle coefficient of rolling friction	0.01

3.4. Numerical parameters and simulation setup

In this work, the EBPM model is implemented in discrete element software EDEM (EDEM, 2017) through the utility of Application Programming Interface (API). To ensure the numerical stability of a simulation using the EBPM model, a number of input parameters should be considered, e.g. time step (Δt), loading rate (L_r) . The time step used in the EBPM simulation was determined based on the critical time step, which is the largest time step to avoid any force transition beyond the nearest neighbouring particles. As noted by Brown et al. (Brown et al., 2014), the critical time step is chosen as the lower of the values of the critical time step for both bonded and non-bonded contacts, as shown in Eq. (14):

$$\Delta t = \xi \min(\Delta t_{bcrit}, \Delta t_{HMcrit}) \tag{14}$$

where ξ is a factor ranging between zero and one. Δt_{bcrit} and Δt_{HMcrit} are the critical time steps for bonded and non-bonded, Hertz-Mindlin contacts, respectively.

The critical time step for a bonded contact is estimated from an assembly of particles using an equivalent single degree of freedom system (Sullivan and Bray, 2003):

$$\Delta t_{bcrit} = 2\sqrt{\frac{m_{pmin}}{K_{bmax}}} \tag{15}$$

where m_{pmin} is the minimum mass of a constituent particle and K_{bmax} is the largest bond stiffness component for that contact.

The critical time step for a non-bonded contact is determined based on the Rayleigh time step, which corresponds to the time taken for a shear wave to propagate through a solid particle (EDEM, 2017):

$$\Delta t_{HMcrit} = \frac{\pi r_p \left(\frac{\rho_p}{G_p}\right)^{0.5}}{(0.1631\upsilon_p + 0.8766)} \tag{16}$$

where r_p is the radius of the smallest constituent particle, ρ_p and G_p are the density and shear modulus of the spherical particles, respectively; υ_p is the Poisson's ratio. The time step is thus determined with the lower value in Eqs. (15) and (16). In this simulation, ξ was selected to be 0.05, leading to the time step calculated as 6.06e-08 s.

The impact velocity is varied from 10 m/s to 60 m/s. As illustrated in Fig. 4, different impact angles are considered for investigating the breakage characteristics under oblique impact conditions. The numerical parameters are shown in Table 4.

4. Results and discussion

4.1. Failure mode, force and velocity evolution during impact

Fig. 5 illustrates the cumulative distribution of broken bonds resulting from compression, tension and shear during the normal impact loading. This classification sheds insights on the dominant failure mechanism. Tension failure accounts for the majority of broken bonds; compressive and shear failures are negligible. This is in accordance with previous research works in this field that show the dominant failure mode of tensile strength (Brown et al., 2014; Kemeny, 1991; Li et al., 2014). The proportion of bonds exhibiting tension failure increases as the impact velocity is increased.

The bond network breakage characteristics at two impact velocities are illustrated by comparing the contact evolutions in Figs. 6 and 7. Fig. 6 shows that the particle remains largely intact at 10 m/s with some internal broken bonds. At the beginning, some local detachments of small pieces occur in the contact zone. Cracks are observed after 0.8 ms but that do not lead to failure of the whole structure. Under 40 m/s impact (Fig. 7), extensive broken bonds (blue) are observed in the contact zone which soon propagate throughout the whole structure. The secondary crack is then generated as the contact evolves, resulting in several pieces of fragments. Four breakage patterns were summarized depending on the impact velocity (Ghadiri et al., 2007). The first is local damage at the impact site, and then by local damage and oblique fracture, and the third by local damage and meridian cracks, and multiple fragments with increased impact velocities (Ghadiri et al., 2007). The

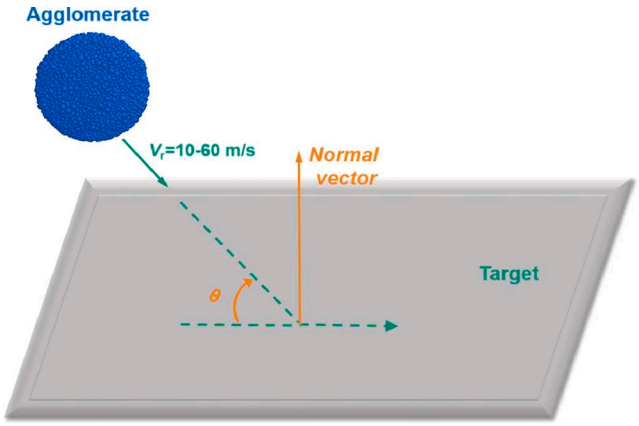

Fig. 4. Illustration of the oblique impact setup (Modified from Khalifa and Breuer (2021)).

Table 4
Global parameters for the DEM simulation of oblique impact.

Parameter	Description	Value
Δt	Time step (s)	6.06e-08
V	Impact velocity (m/s)	10, 20, 30, 40, 60
θ	Impact angle (°)	90, 75, 60, 45, 30

breakage patterns in this work are consistent with previous work (Ghadiri et al., 2007; Thornton et al., 1996). The broken bonds are concentrated at the impact zone, resulting in localized damage at 10 m/s while the broken bonds spread over the whole structure, leading to multiple fragmentations at 40 m/s.

The transition of breakage pattern is further confirmed by comparing the spatial distribution of particle velocity and bond stress considering different impact angles (Figs. 8 -11). When the impact velocity is 10 m/s, velocity gradients appear at the impact sites (Fig. 8). The particle velocity and bond stress structures are almost intact (Figs. 8 and 9), and a fracture plane can only be observed at the impact angle of 90° in Fig. 9. When the impact velocity is v = 40 m/s, more obvious velocity gradients can be observed, and the velocity distribution changes with increased impact angle (Fig. 10). In addition, the area having large bond stress distributions which indicate the occurrence of breakage increases compared with v = 10 m/s (Fig. 11). For both cases, with increased impact angle, the affected region increases, and much more breakage occurs. The observation of breakage behaviors under different impact angles and impact velocities is further quantitatively analyzed in the following sections.

4.2. Damage ratio and breakage ratio

In DEM simulations, particle impact breakage probability is usually quantified by the damage ratio which is defined as the number percentage of broken bonds to the total number of bonds before impact (Thornton et al., 1996). In contrast, particle breakage is experimentally quantified by the breakage ratio which is defined as the ratio of debris mass to the total mass of mother and debris particles. The marked disparity of breakage probability characterization presents a grand challenge in calibrating DEM simulation of impact breakage. As a consequence, very few direct comparisons exist in the literature with respect to breakage results between the experiment and DEM simulation. To address this barrier, a post-processing function to analyse the broken particle size distribution is purposefully developed here.

4.2.1. Damage ratio

In a bonded contact DEM simulation, damage ratio is most widely used to represent the degree of impact breakage (Kafui and Thornton, 1993). The damage ratio is defined as a function of broken bonds as:

$$D_r = \frac{B_0 - B}{B_0} \tag{17}$$

where D_r is the damage ratio, B_0 and B are the numbers of bonded contacts belonging to each individual particle before and after impact, respectively. Note that the damage ratio defined here is used to describe the breakage status at the particle scale which is different to the bond network breakage in Figs. 7-8. In the following, the damage ratio D_r is calculated at a time step of $t = 2$ ms.

The damage ratios for each individual particle within the particle assembly are illustrated in Fig. 12. The simulations indicate the damage ratio for each particle by changing its color from blue to green to red, where blue means that no broken contacts and red means that all the original contacts are broken. As shown in Fig. 12, as the particle color within the particle assembly changes from blue to green to red, this represents the increasing proportion of broken bond contacts for the particle assembly as a whole. The damage ratio distributions clearly describe the breakage pattern evolution from localized damage to

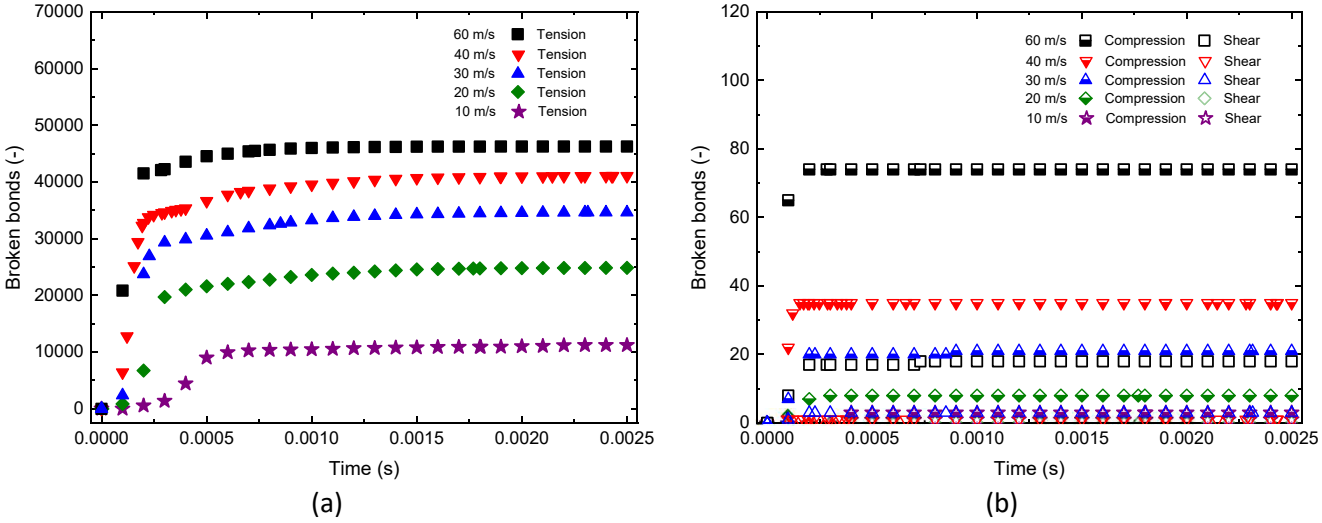

Fig. 5. Failure modes of bonds subjected to normal impact loading (a) tension failure, (b) compression and shear failure.

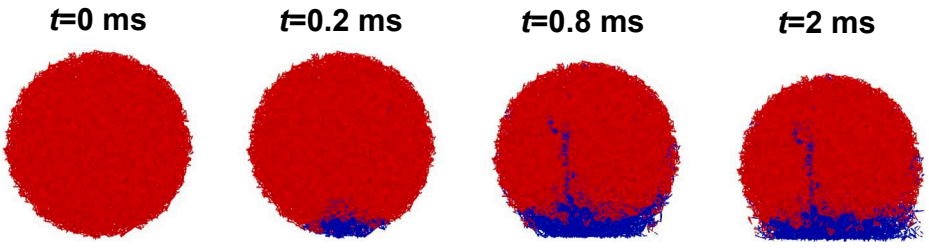

Fig. 6. Surface damage resulting in localized damage at impact velocity of 10 m/s (red = intact bond, blue = broken bond). (For interpretation of the references to color in this figure legend, the reader is referred to the web version of this article.)

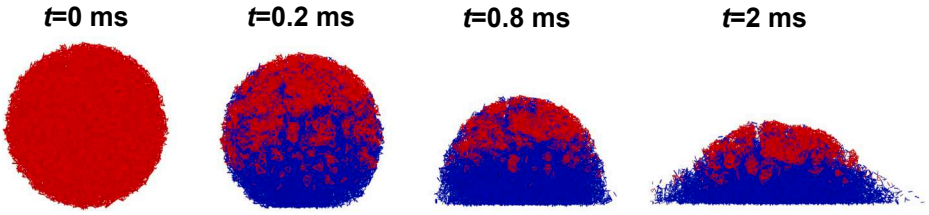

Fig. 7. Cone crack initiated with secondary crack propagation leading to multiple fragmentations at impact velocity of 40 m/s (red = intact bond, blue = broken bond). (For interpretation of the references to color in this figure legend, the reader is referred to the web version of this article.)

multiple fragments with increased impact velocity. This breakage phenomenon is in good agreement with the literature report from (Mishra and Thornton, 2001). Whilst the impact velocity is sufficiently high, no clusters will survive after impact and the agglomerated particle simply collapses as a heap on the impact target, which is exactly as shown in this work for the impact velocity 60 m/s. Nevertheless, the breakage observation is only limited to the input of DEM parameters in this study and further experimental attempts are still required for quantitative comparison.

The average damage ratio for the whole particle assembly is calculated by using the total number of bonded contacts of the whole structure before and after impact. Results are depicted in Fig. 13 for impact velocities ranging from 10 m/s to 60 m/s. The damage ratio rises rapidly as the impact velocity increases from 10 m/s to 60 m/s. For all impact velocities, the damage ratio increases with increased impact angle and eventually levels off after 75° impact angle. The calculated average damage ratios are further compared with the breakage probability that is described in the following section.

4.2.2. *Fragment size distribution and breakage probability*

For performing the fragment size analysis and breakage probability calculation, a method based on the Breadth-First search algorithm (EF, 1959) is developed in this work. This function firstly identifies the ID of the particles forming each cluster based on a node matrix ID and adjacent matrix exported from DEM simulations. The Breadth-First search algorithm shown in Fig. 14 is featured by a loop to check through all the particles in contact detection. This algorithm takes advantage of the bonded contacts between constitutive particles and each contact is assigned with an ID. At every searching iteration, the algorithm will check whether there is a further ID connecting at least one constitutive particle. If the ID is detected, then the identified particle will be assigned within the same cluster of the initial contact. In case of non-existent contact with the preceding particle, a new group membership will be created for partition. The assignment process of neighbouring particles to the existing cluster will be completed until no further contact can be found with the last detected particle. By doing so, the Breadth-First algorithm will establish a series of clusters based on the contact information in Fig. 15, which will be then used for shape fitting and size

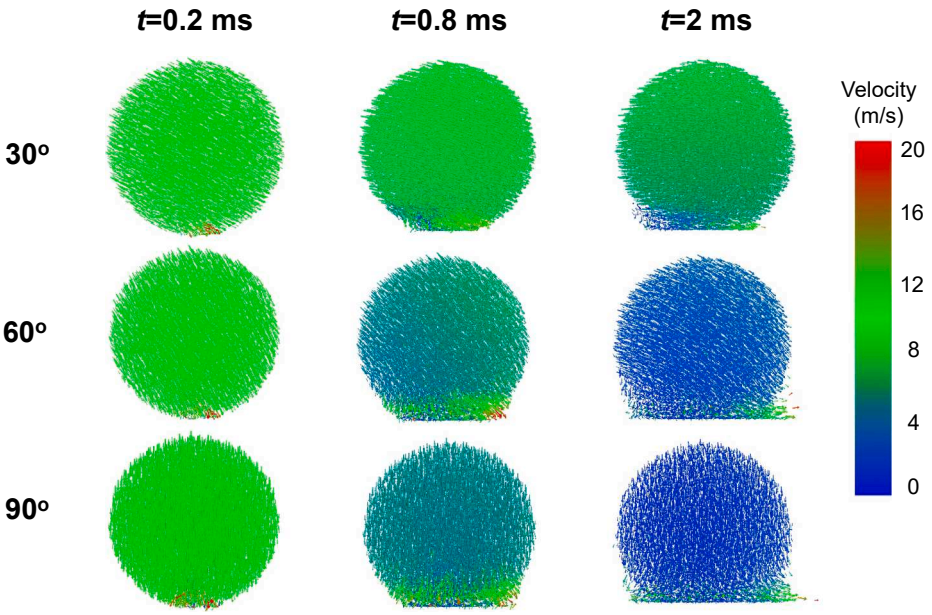

Fig. 8. Spatial distribution of particle velocity under different impact angles under 10 m/s impact.

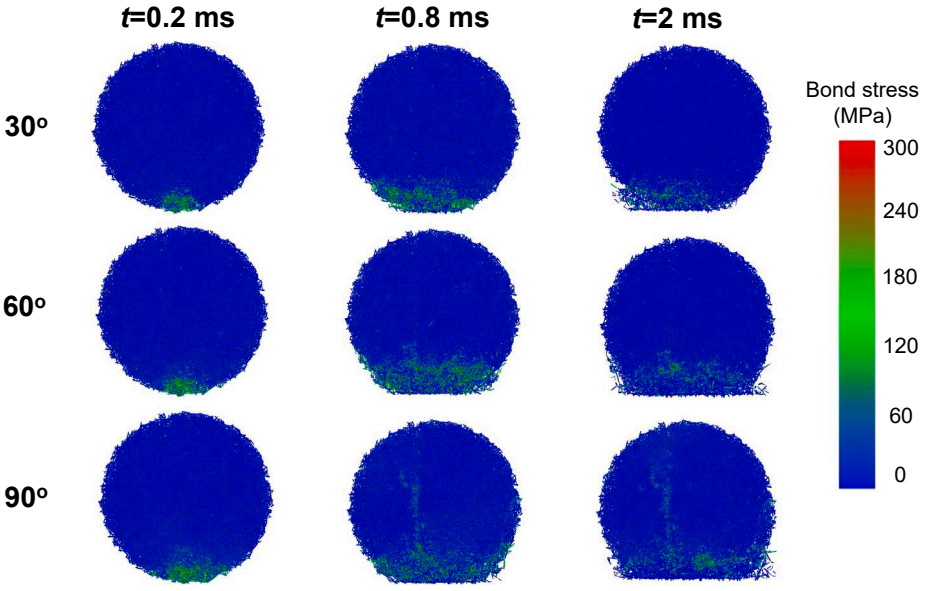

Fig. 9. Bond stress distribution under different impact angles under 10 m/s impact.

analysis in the following.

The effects of different shape fitting such as ellipse, rectangle and circle were discussed (Kumara et al., 2012) and it was found that the ellipse gave the closest size prediction of that measured by sieve analysis. Therefore, the fragment cluster is assumed to have an ellipsoidal shape and the radii of the ellipsoid can be determined through a MATLAB program (Petrov, 2015). The effects of grain size definition were investigated by two methods as a function of ellipsoid fitting (Kumara et al., 2012). In Fig. 16, the grain size can be defined for particles passing parallel to sides of a sieve (D_1) or through the diagonal of a sieve (D_2), respectively:

$$D_1 = \sqrt{0.5(b^2 + c^2)}$$

$$D_2 = b\sqrt{0.5(1 + \alpha^2)} \tag{18}$$

where b and c are the intermediate diameter and shortest diameter of the cluster based on ellipsoid fitting, respectively. α is a constant between the intermediate diameter and shortest diameter of the particle and is assigned as 0.9 in this work. The particle size defined by D_2 is closer to the sieve analysis than that defined by D_1. Hence, D_2 is used in this work to measure the particle size distribution.

By using the Breadth-First search algorithm and ellipsoid fitting approach, the mass of particle clusters and the nominal sizes are calculated separately. Each particle cluster including the detailed individual particle position and particle mass can be identified by using the Breadth-First search algorithm. The mass of each particle cluster can therefore be calculated by summing all the individual particle mass. The ellipsoid fitting function is used to estimate the size of the corresponding particle cluster. After calculating all the particle cluster mass and corresponding size, the size distribution of fragments under different impact conditions is calculated and plotted on a logarithmic plot, as illustrated in Fig. 17. In this figure, the size of fragment clusters l is

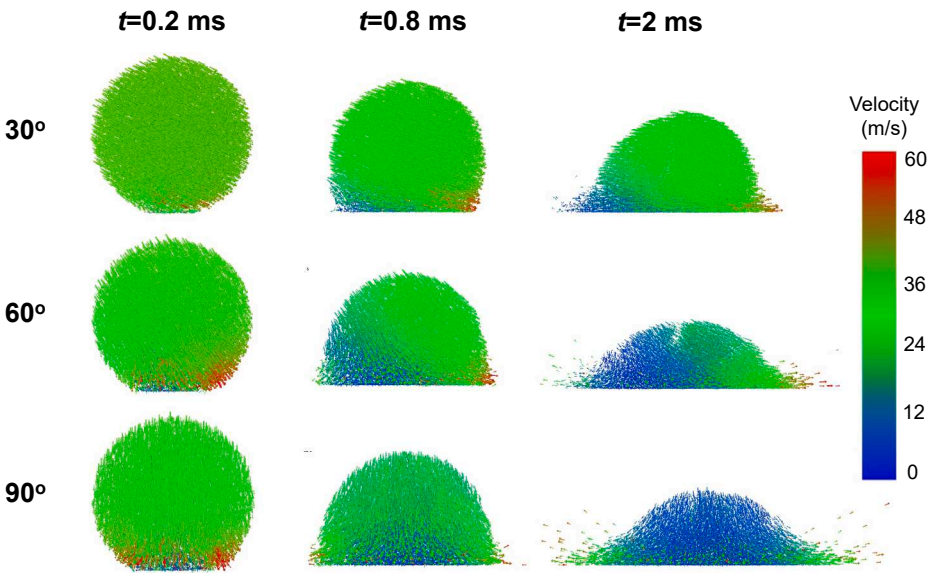

Fig. 10. Spatial distribution of particle velocity under different impact angles under 40 m/s impact.

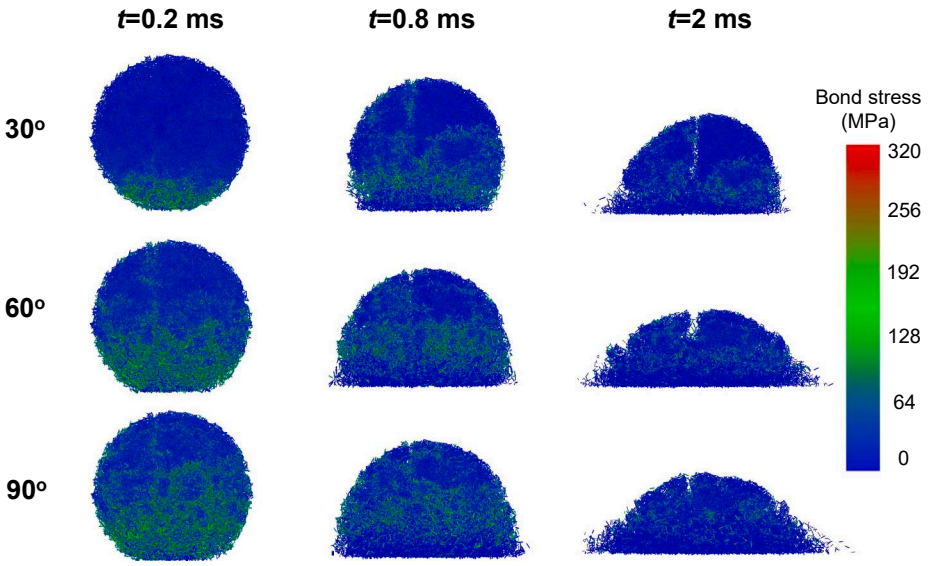

Fig. 11. Bond stress distribution under different impact angles under 40 m/s impact.

normalised by the size of the original particle assembly l_0. The ordinate represents the cumulative mass fraction undersize. In general, the breakage increases with increased impact angle and impact velocity. It can also be observed that the curves for 75° and 90° impact angles are very close and even overlap with each other.

For all cases, the size distribution curves have two different regions with a sudden increase in the end. With increased impact angle and velocity, the gap between these two regions becomes narrower and tends to disappear when the impact velocity is 60 m/s with 75° and 90° impact angles. The size distribution curves reported here are in agreement with the experimental results of agglomerates under impact conditions (Subero and Ghadiri, 2001): the very low slope on the left hand side of the figure corresponds to the small fragments or debris, and slope difference on the right hand side indicates the transition to the mother fragments.

The breakage ratio is defined as the ratio of debris mass to the initial mass of the whole particle assembly. The cumulative mass fraction of debris fragments can be easily calculated from the size distribution plot in Fig. 17. The calculated breakage probabilities under different conditions are given in Fig. 18. The breakage probability has a very similar variation tendency with the damage ratio in Fig. 13 with increased impact velocity and impact angle. As can be expected, the breakage probability increases with the impact velocity. However, the damage ratio in Fig. 13 is much higher than the breakage ratio measured for the same impact velocity under the single particle impact test (Fig. 19).

As mentioned above, the direct comparison of damage ratio and breakage ratio of particle impact breakage from DEM simulation is typically unavailable in the literature. As a result, it will be of scientific merit to make direct comparison between damage ratio and breakage ratio under the identical impact circumstances shown in Fig. 18. Given the breakage results by DEM, the damage ratio is always larger than the breakage ratio under the same impact conditions. The reason for the difference is due to the fact that the damage ratio is defined by the number of broken bonds while the breakage propensity is defined by the resulting volume loss due to impact based on particle size distribution. This infers that evaluation of breakage using damage ratio tends to overestimate the breakage probability compared to breakage ratio. In

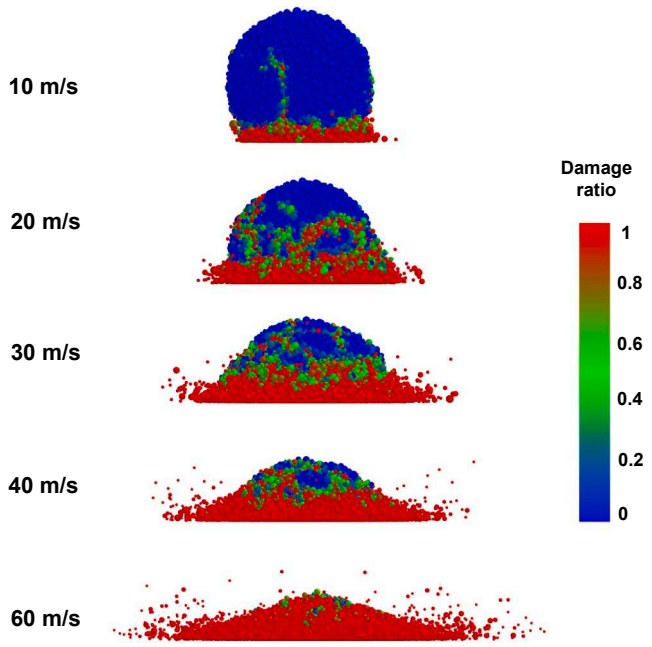

Fig. 12. Damage ratio of individual particles within particle assembly under different impact velocities subjected to normal impact loading. Note that blue means no bonds have been broken, green means half bond contacts have been broken and red means all bonded contacts have been broken. (For interpretation of the references to color in this figure legend, the reader is referred to the web version of this article.)

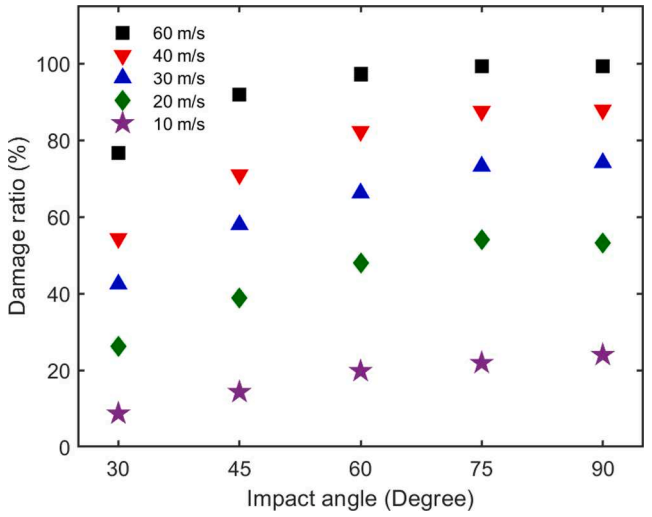

Fig. 13. Average damage ratios for particles as a function of impact angle ranging from 10 m/s to 60 m/s.

particular, the discrepancy between damage ratio and breakage ratio increasingly widens as the impact angle is decreased.

The calculation of breakage probability results based on DEM simulations and fragments size analysis provides a promising instrument to compare with experimental results, and to develop and validate breakage models in a straightforward way.

5. Oblique impact breakage master curve

5.1. An oblique impact model

The existing breakage models only consider the contribution of normal impact and therefore the tangential velocity component under oblique impact is typically ignored. Although a series of breakage probability models were previously assessed for either single particle breakage or a milling process, the effect of impact angle has not ever been justified in an oblique impact breakage model. The experimental and simulation single impact results demonstrate that tangential velocity exerts a significant influence on the breakage propensity (Khanal and Tomas, 2009; Salman et al., 2003; Ye et al., 2021). As a result, developing an oblique impact model to incorporate tangential velocity under oblique impact is deemed imperative. To tackle this challenge, an oblique impact model considering the effect of impact angle has been developed and presented in details by Wang et al. (Wang et al., 2021a). As the focal point of this work is intended for oblique impact, only the relevant part of the model development is reviewed as below.

Given an impact angle θ, the normal velocity v_n gives

$$v_n = v\sin\theta \tag{19}$$

The tangential velocity v_t gives

$$v_t = v\cos\theta \tag{20}$$

The normal velocity v_n and tangential velocity v_t result in the normal impact force F_n and the tangential impact force F_t. However, the relationship between v_t and F_t, and that between v_n and F_n, are not necessarily identical. F_t is restricted by the dynamic friction between the particle and the impact surface, namely μF_n that is in turn associated with $\mu v\sin\theta$. A large tangential velocity but without sufficient frictional force between particle and impact surface may not result in any damage. An 'effective' tangential velocity which can result in particle damage can be expressed in the form of:

$$v_{te} = \mu v\sin\theta\cos\theta \tag{21}$$

This indicates that the contribution of the tangential component to damage will be zero for both the case of normal impact (as there is no tangential velocity), and the case of a complete tangential impact. This is due to the fact that the particle travels parallel to the impact surface without any contact force between them.

A total resultant force that combines the normal and tangential forces can be expresses as,

$$F = \sqrt{F_n^2 + F_t^2} \tag{22}$$

However, using the total force could be misleading because damages caused by F_n and F_t are different even if their value and time characteristics are identical. As a simple treatment before further understanding is achieved, here we assume that the combined effect of F_n and F_t on damage is the same as that caused by an 'equivalent' normal force F_e and it can be expressed as,

$$F_e = \sqrt{F_n^2 + \beta^2 F_t^2} \tag{23}$$

where β is a coefficient that incorporates the contribution of F_t.

Considering Eqs. (22) and (23) with the force analogy, an 'equivalent' normal impact velocity can be defined as,

$$v_{eq} = \sqrt{v_n^2 + \beta^2 v_{te}^2} \tag{24}$$

Substituting Eq. (19) for normal velocity and Eq. (21) for effective tangential velocity into Eq. (24), it evolves

$$v_{eq} = v\sqrt{\sin^2\theta + \psi^2\sin^2\theta\cos^2\theta} \tag{25}$$

in which $\psi = \beta\mu$ reflects the synergic effects of frictional behaviour and various above-mentioned relationships .

Eq. (25) infers that the high impact velocity with a smaller impact angle can result in the same amount of breakage from low impact velocity with a larger impact angle, given the same value of equivalent

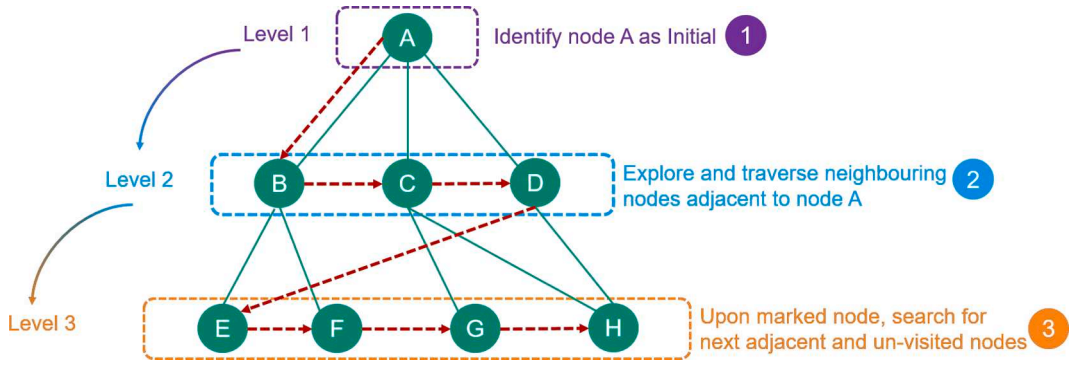

Fig. 14. Schematic of breadth-first search.

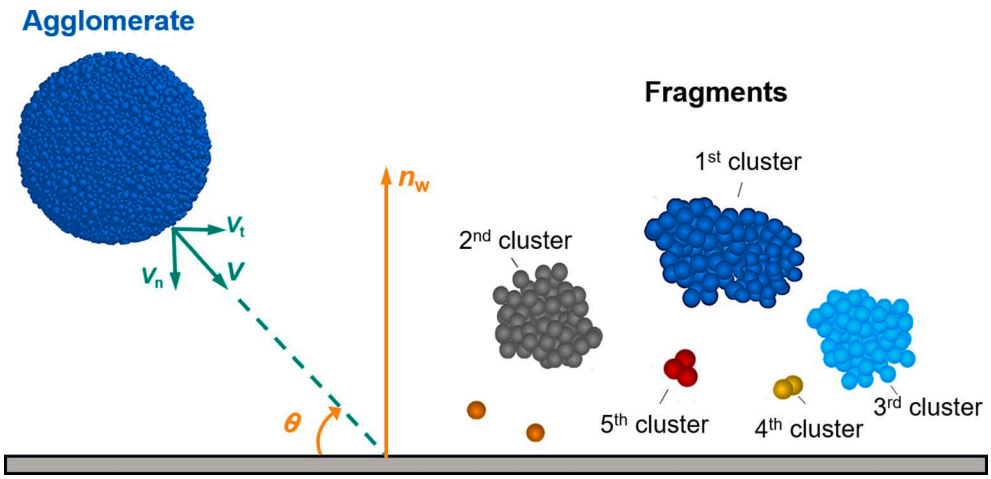

Fig. 15. Schematic of particle cluster following oblique impact, the particles with bonded contacts are classified as one cluster; n_w denotes normal vector on the impact target (Modified from Khalifa and Breuer (2021)).

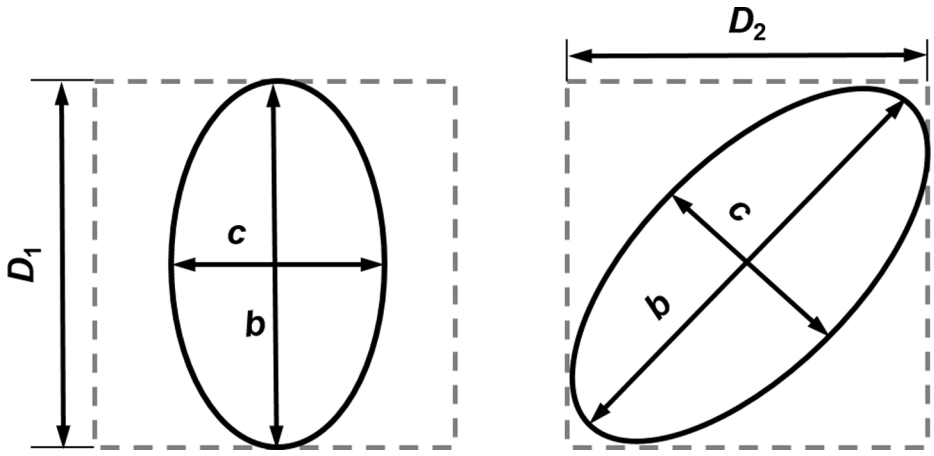

Fig. 16. Schematic outline of particle size definition based on ellipsoid fitting (a) parallel to sides and (b) through diagonal of square sieve (Modified from Kumara et al. (2012)).

velocity. The key message in Eq. (25) is that the magnitude of equivalent velocity is between the normal velocity $v_n = v\sin\theta$ and the impact velocity v. This is particularly important in the oblique impact circumstance where the impact angle is considered in equivalent velocity. This is because only the normal velocity cannot adequately induce the breakage probability whilst excluding the contribution of tangential velocity. However, the equivalent velocity outworks the impact velocity under oblique impact. The equivalent velocity in Eq. (25) is generally applicable to any existing breakage models and a simple treatment by replacing the normal velocity with equivalent velocity will be shown below in establishing a unified breakage curve for breakage data with various impact angles.

5.2. Master curve of DEM oblique impact

To investigate the applicability of equivalent velocity under oblique

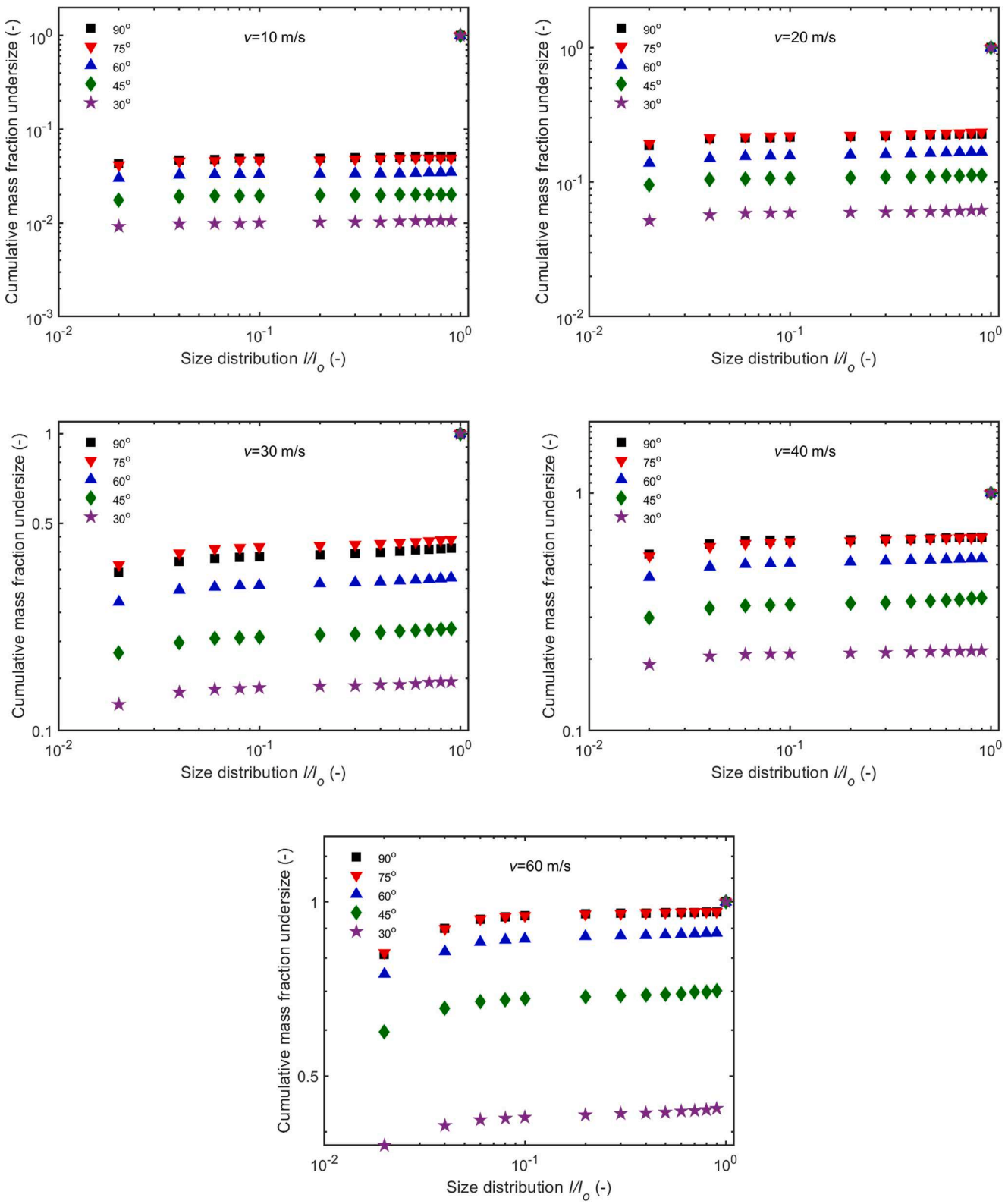

Fig. 17. Comparison of the size distribution of the fragments from DEM simulations under different impact conditions.

impact, the first step is to choose an impact breakage model where the fitting parameters can be determined under normal impact loadings. Secondly, the equivalent velocity is substituted into the breakage model to replace the nominal term associated with either impact velocity or impact energy. The DEM simulation of impact breakage in Fig. 18 clearly demonstrates a fragmentation curve when the impact velocity is increased from 10 m/s to 60 m/s. Hence, the chosen breakage model in this work is Vogel and Peukert model (Vogel and Peukert, 2003) and it gives:

$$P_x = 1 - exp\{-f_{Mat}xk(W_{m,kin} - W_{m,min})\} \tag{26}$$

where P_x is breakage probability; $W_{m,kin}$ is mass-specific kinetic energy;

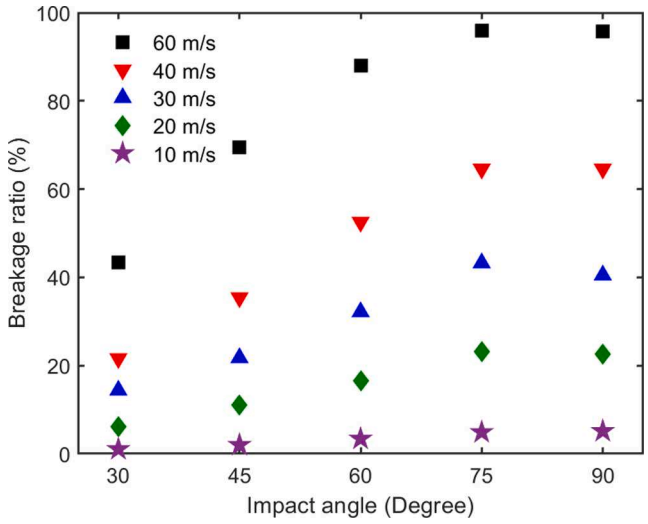

Fig. 18. Breakage ratio for particles as a function of impact angle ranging from 10 m/s to 60 m/s.

x and k are particle size and impact number. In this work, $x = 50$ mm, and $k = 1$. f_{Mat} and $W_{m,min}$ are the material dependent properties.

The reason to choose Vogel and Peukert model is because of its mechanistic and statistical foundations to account for impact breakage. Most importantly, a breakage master curve was successfully established in unifying numerous factors such as impact energy, particle size and impact number. It will be of scientific merit to explore whether the proposed equivalent velocity can result in a breakage master curve in the oblique impact environment. To that end, the first step is to find the optimal values of two material-dependent parameters f_{Mat} and $W_{m,min}$ based on the normal impact breakage data. The second step is to replace $W_{m,kin} = v^2/2$ as equivalent velocity based energy format $v_{eq}^2/2$ in Eq. (26) and to achieve the optimal value of ψ based on the breakage data under the four oblique impact angles 75°, 60°, 45°, and 30°. The fitting parameters in Vogel and Peukert model are optimized as $f_{Mat} = 0.037$ kg/Jm and $W_{m,min} = 102.5$ J/kg based on the normal impact breakage data. Fig. 20 displays the breakage ratio as a function of equivalent velocity with the optimal value of $\psi = 0.27$. The master curve is observed to well capture the breakage trend where the breakage ratios under all the impact angles are simultaneously unified.

6. Conclusions

In this work, for the first time, a particle breakage master curve of oblique impact has been established using a DEM bonded contact model. The assembled particle is impacted under five impact angles and increased impact velocities. The transition of breakage patterns from localized damage to multiple fragments is observed with increased impact velocities, showing qualitative agreement with the literature results. The main failure mode of bonds is mainly failed by tension whilst compressive and shear failures are trivial.

Two longstanding issues in the particle impact breakage have been properly addressed through this study. Previously, there is a lack of straightforward comparison between the breakage ratio in experiments and damage ratio in DEM simulation. To overcome this issue, a Breadth-First Search Algorithm is developed to analyse the fragment size distribution after impact breakage. By doing so, the same breakage criterion can be applied between DEM simulation and experimental characterisation. The second issue is the futility of existing breakage models in predicting the breakage probability under oblique impact. In other words, there falls short of a unified breakage master curve to predict the impact breakage probability under oblique impact circumstances. In recognition of this shortfall, the equivalent velocity is proposed to address the deficiency of existing models where only the contribution of normal velocity is considered. The equivalent velocity specific to oblique impact loading is proposed to successfully establish the unified breakage master curve by mobilising the dynamic friction.

Using the equivalent velocity combined with DEM, a breakage master curve is theoretically constructed for various impact angles. By further experimental validation, the developed algorithm for particle size distribution from DEM results can be applied to realistic processes where oblique impact breakage is prevailing such as the rock impact breakage in geotechnical engineering.

Data availability

The code developed to post-process the bonded contact data is available from the corresponding author upon request.

CRediT authorship contribution statement

Li Ge Wang: Writing – original draft, Methodology, Software. **Ruihuan Ge:** Conceptualization, Supervision, Writing – review & editing. **Xizhong Chen:** Data curation, Formal analysis, Resources.

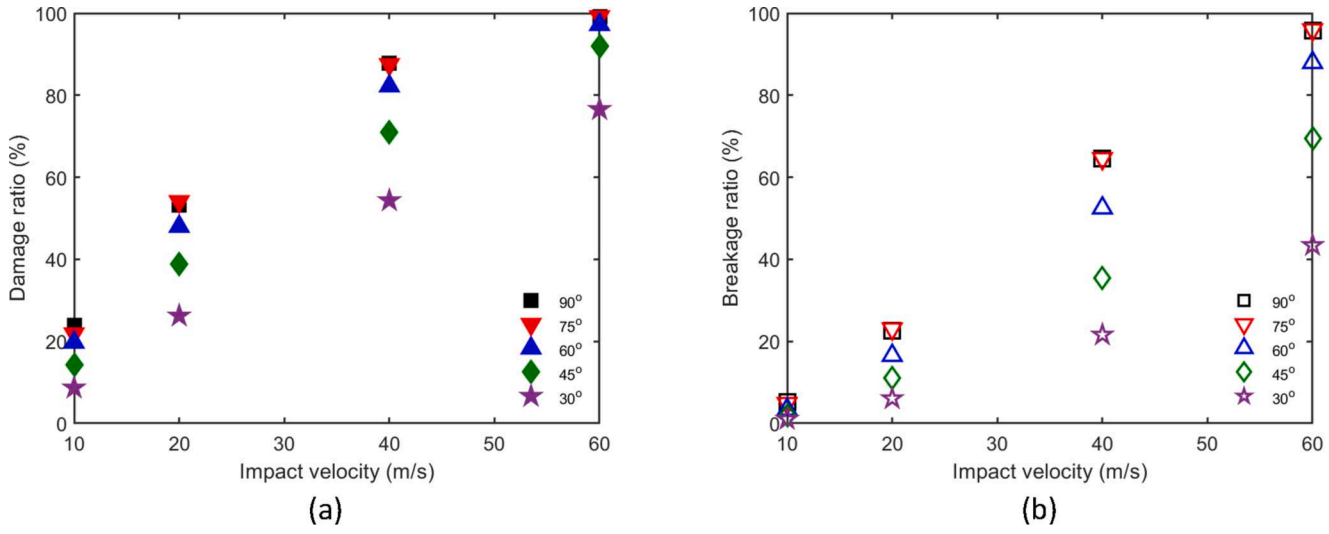

Fig. 19. Comparison of (a) damage ratio and (b) breakage ratio under various impact velocities and impact angles.

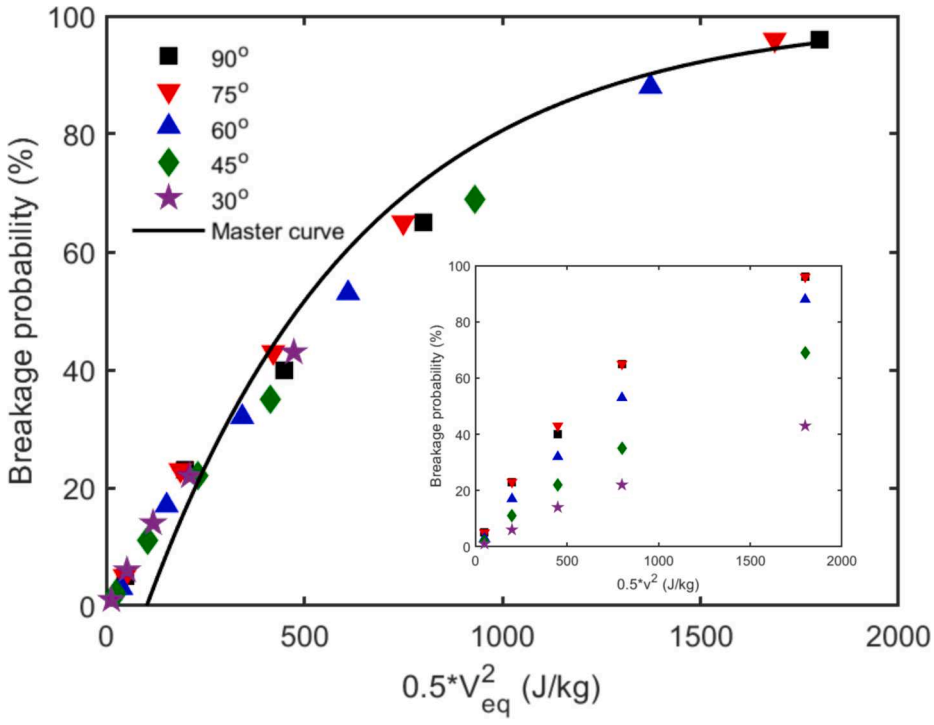

Fig. 20. Unified breakage master curve of breakage ratio using the equivalent velocity.

Declaration of Competing Interest

The authors declare that they have no known competing financial interests or personal relationships that could have appeared to influence the work reported in this paper.

Acknowledgement

The first author would like to appreciate Innovate UK to fund Knowledge Transfer Partnership (KTP) Grant No. 158229 between University of Sheffield and Process Systems Enterprise, which enables this explorative work to be finalised over the KTP stint.

Appendix A

To demonstrate the fidelity of the calibrated parameters. The uniaxial compressive strength (UCS) test was firstly performed. The compressive strength of the concrete specimen is calculated as 27.9 MPa, which is the same with the result from (Brown, 2013). Following the UCS test, the Brazilian tensile strength (BTS) test is intentionally carried out using the same set of calibrated parameters to measure the tensile strength of a concrete specimen shown below. The tensile strength of the concrete specimen is thus calculated as 4.9 MPa following the equation below:

$$BTS = \frac{2L}{\pi Dt} \tag{1}$$

where L is the axial failure force; D and t are the specimen diameter and thickness ($D = 100$mm, $t = 200$mm).

With an empirical relationship between compressive and tensile strength for brittle concrete-like or rock-like materials (Chhorn et al., 2018), the bulk tensile strength is shown to be 17.6% of the compressive strength, which falls in the common range of tensile strength for conventional brittle materials.

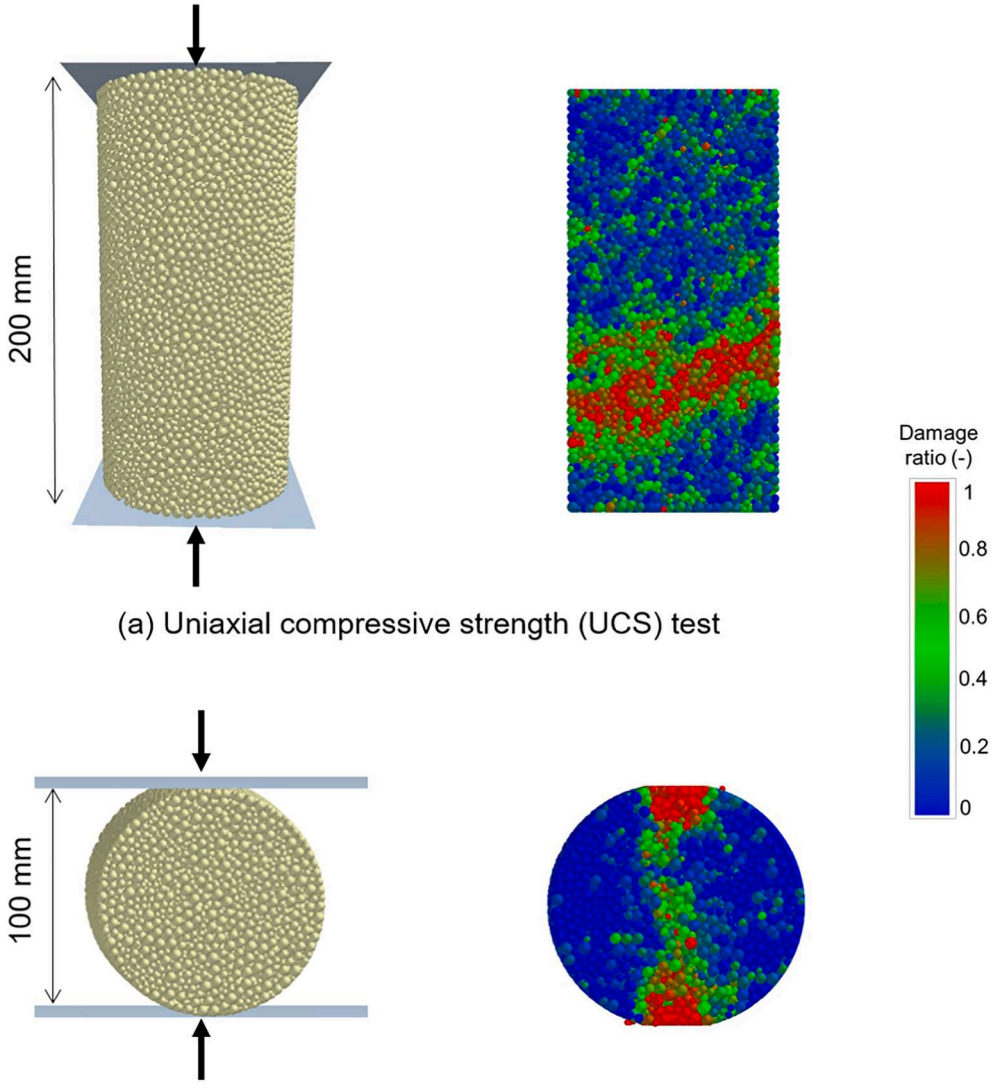

References

Brown, N.J., 2013. Discrete Element Modelling of Cementitious Materials. The University of Edinburgh.

Brown, N.J., Chen, J.F., Ooi, J.Y., 2014. A bond model for DEM simulation of cementitious materials and deformable structures. Granul. Matter 16, 299–311. https://doi.org/10.1007/s10035-014-0494-4.

Carmona, H.A., Wittel, F.K., Kun, F., Herrmann, H.J., 2008. Fragmentation processes in impact of spheres. Phys. Rev. E – Stat. Nonlinear, Soft Matter Phys. 77, 1–10. https://doi.org/10.1103/PhysRevE.77.051302.

Chhorn, C., Hong, S.J., Lee, S.W., 2018. Relationship between compressive and tensile strengths of roller-compacted concrete. J. Traffic Transp. Eng. (English Ed.) 5, 215–223. https://doi.org/10.1016/j.jtte.2017.09.002.

Coetzee, C.J., 2017. Review: calibration of the discrete element method. Powder Technol. 310, 104–142. https://doi.org/10.1016/j.powtec.2017.01.015.

EF, M., 1959. The shortest path through a maze. In: Proceedings of an International Symposium on the Theory of Switching. pp. 285–292.

Ergenzinger, C., Seifried, R., Eberhard, P., 2011. A discrete element model to describe failure of strong rock in uniaxial compression. Granul. Matter 13, 341–364. https://doi.org/10.1007/s10035-010-0230-7.

Evans, A.G., Gulden, M.E., Rosenblatt, M., 1978. Impact damage in brittle materials in the elastic-plastic response regime. Proc. R Soc. A Math. Phys. Eng. Sci. 361, 343–365. https://doi.org/10.1098/rspa.1978.0106.

EDEM 2017 User Guide. DEM Solution Ltd., Edinburgh, UK, 2016.

Evans, A.G., Wilshaw, T.R., 1976. Quasi-static solid particle damage in brittle solids – I. Observations, analysis and implications. Acta Metall. 24, 939–956. https://doi.org/10.1016/0001-6160(76)90042-0.

Ge, R., Ghadiri, M., Bonakdar, T., Hapgood, K., 2017. 3D printed agglomerates for granule breakage tests. Powder Technol. 306, 103–112. https://doi.org/10.1016/j.powtec.2016.10.070.

Ge, R., Ghadiri, M., Bonakdar, T., Zheng, Q., Zhou, Z., Larson, I., Hapgood, K., 2020. Deformation of 3D printed agglomerates: multiscale experimental tests and DEM simulation. Chem. Eng. Sci. 217, 115526. https://doi.org/10.1016/j.ces.2020.115526.

Ge, R., Wang, L., Zhou, Z., 2019. DEM analysis of compression breakage of 3D printed agglomerates with different structures. Powder Technol. 356, 1045–1058. https://doi.org/10.1016/j.powtec.2019.08.113.

Gentilini, C., Govoni, L., de Miranda, S., Gottardi, G., Ubertini, F., 2012. Three-dimensional numerical modelling of falling rock protection barriers. Comput. Geotech. 44, 58–72. https://doi.org/10.1016/j.compgeo.2012.03.011.

Ghadiri, M., Moreno-Atanasio, R., Hassanpour, A., Antony, S.J., 2007. Chapter 19 analysis of agglomerate breakage. Handb. Powder Technol. 12, 837–872. <https://doi.org/10.1016/S0167-3785(07)12022-4>.

Ghadiri, M., Zhang, Z., 2002. Impact attrition of particulate solids. Part 1: A theoretical model of chipping. Chem. Eng. Sci. 57, 3659–3669. https://doi.org/10.1016/S0009-2509(02)00240-3.

Giacomini, A., Buzzi, O., Renard, B., Giani, G.P., 2009. Experimental studies on fragmentation of rock falls on impact with rock surfaces. Int. J. Rock Mech. Min. Sci. 46, 708–715. https://doi.org/10.1016/j.ijrmms.2008.09.007.

Gilvari, H., de Jong, W., Schott, D.L., 2020. Breakage behavior of biomass pellets: an experimental and numerical study. Comput. Part. Mech. <https://doi.org/10.1007/s40571-020-00352-3>.
Jiang, M., Zhang, F., Sun, Y., 2014. An evaluation on the degradation evolutions in three constitutive models for bonded geomaterials by DEM analyses. Comput. Geotech. 57, 1–16. https://doi.org/10.1016/j.compgeo.2013.12.008.
Kafui, K.D., Thornton, C., 1993. Powders & Grains 93, The Proceedings of the 2nd International Conference on Micromechanics of Granular Media. Balkema, Rotterdam, pp. 401–406.
Kemeny, J.M., 1991. A model for non-linear rock deformation under compression due to sub-critical crack growth. Int. J. Rock Mech. Min. Sci. 28, 459–467. https://doi.org/10.1016/0148-9062(91)91121-7.
Khalifa, A., Breuer, M., 2021. An efficient model for the breakage of agglomerates by wall impact applied to Euler-Lagrange LES predictions. Int. J. Multiph. Flow 103625. https://doi.org/10.1016/j.ijmultiphaseflow.2021.103625.
Khanal, M., Tomas, J., 2009. Oblique impact simulations of high strength agglomerates. Adv. Powder Technol. 20, 150–157. https://doi.org/10.1016/j.apt.2008.06.001.
Kumara, G.H.A., Hayano, K., Ogiwara, K., 2012. Image analysis techniques on evaluation of particle size distribution of gravel. Int. J. GEOMATE 3, 290–297.
Kun, F., Herrmann, H.J., 1999. Transition from damage to fragmentation in collision of solids. Phys. Rev. E 59, 2623–2632. https://doi.org/10.1103/PhysRevE.59.2623.
Kun, F., Herrmann, H.J., 1996. A study of fragmentation processes using a discrete element. Comput. Methods Appl. Mech. Eng. 138, 3–18.
Li, X.J., Yang, W.M., Wang, L.G., Butler, I.B., 2014. Displacement forecasting method in brittle crack surrounding rock under excavation unloading incorporating opening deformation. Rock Mech. Rock Eng. 47 https://doi.org/10.1007/s00603-014-0599-4.
Li, Z.P., Wang, L.G., Chen, W., Chen, X., Liu, C., Yang, D., 2020. Scale-up procedure of parameter estimation in selection and breakage functions for impact pin milling. Adv. Powder Technol. 31, 3507–3520.
Meier, M., John, E., Wieckhusen, D., Wirth, W., Peukert, W., 2009. Influence of mechanical properties on impact fracture: prediction of the milling behaviour of pharmaceutical powders by nanoindentation. Powder Technol. 188, 301–313. https://doi.org/10.1016/j.powtec.2008.05.009.
Mindlin, R.D., Deresiewicz, H., 1953. Elastic spheres in contact under varying oblique forces. Appl. Mech. 327–344.
Mishra, B.K., Thornton, C., 2001. Impact breakage of particle agglomerates. Int. J. Miner. Process. 61, 225–239. https://doi.org/10.1016/S0301-7516(00)00065-X.
Moreno, R., Ghadiri, M., Antony, S.J., 2003. Effect of the impact angle on the breakage of agglomerates: a numerical study using DEM. Powder Technol. 130, 132–137. https://doi.org/10.1016/S0032-5910(02)00256-5.
Ouyang, Y., Yang, Q., Chen, X., 2017. Bonded-particle model with nonlinear elastic tensile stiffness for rock-like materials. Appl. Sci. 7 https://doi.org/10.3390/app7070686.
Petrov, Y., 2015. Ellipsoid fit. Matlab Cent.
Potapov, A.V., Campbell, C.S., 1994. Computer simulation of particle breakage. Powder Technol. 81, 207–216. https://doi.org/10.1016/0032-5910(94)02907-5.
Potyondy, D.O., Cundall, P.A., 2004. A bonded-particle model for rock. Int. J. Rock Mech. Min. Sci. 41, 1329–1364. https://doi.org/10.1016/j.ijrmms.2004.09.011.
Przemieniecki, 1968. Theory of Matrix Structural Analysis. McGraw-Hill, New York.
Ruiz-Carulla, R., Corominas, J., Mavrouli, O., 2017. A fractal fragmentation model for rockfalls. Landslides 14, 875–889. https://doi.org/10.1007/s10346-016-0773-8.
Salman, A., Reynolds, G., Hounslow, M., 2003a. Particle impact breakage in particulate processing. KONA Powder Part. J. 21, 88–99. https://doi.org/10.14356/kona.2003012.
Salman, A.D., Fu, J., Gorham, D.A., Hounslow, M.J., 2003b. Impact breakage of fertiliser granules. Powder Technol. 130, 359–366. https://doi.org/10.1016/S0032-5910(02)00237-1.
Salman, A.D., Gorham, D.A., Verba, A., 1995. A study of solid particle failure under normal and oblique impact. Wear 186–187, 92–98. https://doi.org/10.1016/0043-1648(95)07140-7.
Shen, Z., Jiang, M., Thornton, C., 2016. DEM simulation of bonded granular material. Part I: Contact model and application to cemented sand. Comput. Geotech. 75, 192–209. https://doi.org/10.1016/j.compgeo.2016.02.007.
Subero, J., Ghadiri, M., 2001. Breakage patterns of agglomerates. Powder Technol. 120, 232–243. https://doi.org/10.1016/S0032-5910(01)00276-5.
Sullivan, C.O., Bray, J.D., 2003. Selecting a suitable time step for discrete element simulations that use the central difference time integration scheme. https://doi.org/10.1108/02644400410519794.
Tavares, L.M., King, R.P., 1998. Single-particle fracture under impact loading. Int. J. Miner. Process. 54, 1–28. https://doi.org/10.1016/S0301-7516(98)00005-2.
Thornton, C., Ciomocos, M.T., Adams, M.J., 1999. Numerical simulations of agglomerate impact breakage. Powder Technol. 105, 74–82. https://doi.org/10.1016/S0032-5910(99)00120-5.
Thornton, C., Yin, K.K., Adams, M.J., 1996. Numerical simulation of the impact fracture and fragmentation of agglomerates. J. Phys. D Appl. Phys. 29, 424+.
Timoshenko, S.P., 1922. On the transverse vibrations of bars of uniform cross-section. Philos. Mag. 43, 125–131.
Tong, Z.B., Yang, R.Y., Chu, K.W., Yu, A.B., Adi, S., Chan, H.K., 2010. Numerical study of the effects of particle size and polydispersity on the agglomerate dispersion in a cyclonic flow. Chem. Eng. J. 164, 432–441. https://doi.org/10.1016/j.cej.2009.11.027.
Tong, Z.B., Yang, R.Y., Yu, A.B., Adi, S., Chan, H.K., 2009. Numerical modelling of the breakage of loose agglomerates of fine particles. Powder Technol. 196, 213–221. https://doi.org/10.1016/j.powtec.2009.08.001.
Tsuji, Y., Tanaka, T., Ishida, T., 1992. Lagrangian numerical simulation of plug flow of cohesionless particles in a horizontal pipe. Powder Technol. 71, 239–250. https://doi.org/10.1016/0032-5910(92)88030-L.
Valera, R.R., Morales, I.P., Vanmaercke, S., Morfa, C.R., Cortés, L.A., Casañas, H.D.G., 2015. Modified algorithm for generating high volume fraction sphere packings. Comput. Part. Mech. 2, 161–172. https://doi.org/10.1007/s40571-015-0045-8.
Vogel, L., Peukert, W., 2003. Breakage behaviour of different materials – construction of a mastercurve for the breakage probability. Powder Technol. 129, 101–110. https://doi.org/10.1016/S0032-5910(02)00217-6.
Wang, L.G., Chen, J.-F., Ooi, J.Y., 2021a. A breakage model for particulate solids under impact loading. Powder Technol. 394, 669–684. https://doi.org/10.1016/j.powtec.2021.08.056.
Wang, L.G., Ge, R., Chen, X., Zhou, R., Chen, H.M., 2021b. Multiscale digital twin for particle breakage in milling: from nanoindentation to population balance model. Powder Technol. 386, 247–261. https://doi.org/10.1016/j.powtec.2021.03.005.
Ye, Y., Zeng, Y., Cheng, S., Sun, H., Chen, X., 2021. Computers and geotechnics numerical investigation of rock sphere breakage upon oblique impact: effect of the contact friction coefficient and impact angle. Comput. Geotech. 136, 104207. https://doi.org/10.1016/j.compgeo.2021.104207.
Zhu, Z.-H., Yin, J.-H., Ouyang, C.-J., Tan, D.-Y., Qin, J.-Q., 2020. Modeling a flexible ring net with the discrete element method. J. Eng. Mech. 146, 04019120. https://doi.org/10.1061/(asce)em.1943-7889.0001707.